HHS Public Access

Author manuscript

ACS Nano. Author manuscript; available in PMC 2017 January 27.

Published in final edited form as:

ACS Nano. 2016 April 26; 10(4): 4020–4030. doi:10.1021/acsnano.5b05396.

Ion-switchable quantum dot FRET rates in ratiometric potassium sensors

Timothy T. Ruckh[1], **Christopher G. Skipwith**[1], **Wendi Chang**[2], **Vladimir Bulovic**[2], **Polina Anikeeva**[3], and **Heather A. Clark**[1,*]

[1]Department of Pharmaceutical Sciences, Northeastern University, 360 Huntington Ave, Boston, MA 02115

[2]Department of Electrical Engineering, Massachusetts Institute of Technology, 77 Massachusetts Avenue, Cambridge, MA 02139

[3]Department of Materials Science and Engineering, Massachusetts Institute of Technology, 77 Massachusetts Avenue, Cambridge, MA 02139

Abstract

The tools for optically imaging cellular potassium concentrations in real-time are currently limited to a small set of molecular indicator dyes. Quantum dot-based nanosensors are more photostable and tunable than organic indicators, but previous designs have fallen short in size, sensitivity, and selectivity. Here we introduce a small, sensitive, and selective nanosensor for potassium measurements. A dynamic quencher modulates the fluorescence emitted by two different quantum dot species to produce a ratiometric signal. We characterized the potassium-modulated sensor properties and investigated the photonic interactions within the sensors. The quencher's protonation changes in response to potassium, which changes its Förster radiative energy transfer rate and the corresponding interaction radii with each quantum dot species. The nanosensors respond to changes in potassium concentrations typical of the cellular environment, and thus provide a promising tool for imaging potassium fluxes during biological events.

TOC image

*To whom correspondence should be directed: H.clark@neu.edu.

Author contributions

TTR and HAC conceived of the work. TTR, CGS, and WC performed experiments. TTR, CGS, WC, HAC and PA analyzed data. All authors were involved with manuscript preparation

Competing financial interests

The authors declare no competing financial interests.

Supporting Information

Extended characterization of nanosensor characterization, time-resolved spectroscopy, and *in situ* calibrations are included in supporting information. This material is available free of charge via the Internet at http://pubs.acs.org.

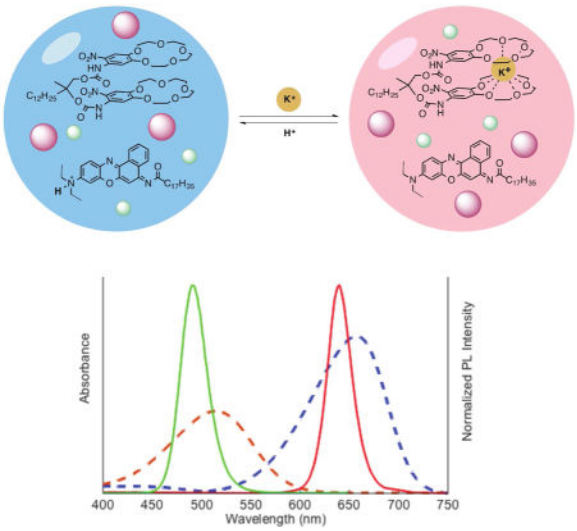

Real-time ion imaging in cellular systems requires analytical tools with high selectivity and sensitivity due to the complex environment. Designing fluorescent reporters that selectively measure sodium or potassium has been particularly difficult[1] despite significant interest in capturing the spatio-temporal patterns in transmembrane ion currents that regulate cell behaviors for both excitable[2] and non-excitable cells[3]. In contrast to extensively optimized small-molecule[4] and genetically-encoded calcium indicators[5], dyes such as sodium-binding benzofuran isophthalate (SBFI) and potassium-binding benzofuran isophthalate (PBFI) are limited by low sensitivity, poor selectivity, and low photoluminescence quantum yield (PLQY)[1b]. A few previous reports using sodium indicators have successfully imaged the spatio-temporal features of sodium fluxes during action potential firing in neurons[1b, 6], but widespread adoption has been limited by the aforementioned problems.

Optode-based nanosensors overcome many of the challenges necessary for measuring ions in biological systems[7]. In the optode platform, hydrophobic optode components are contained within a plasticizer nano-emulsion and stabilized by a biocompatible surfactant. The hydrophobic sensing components for a potassium nanosensor consist of a colorimetric pH indicator, a potassium-binding crown ether, and an anion[7a, 7b], termed the chromoionophore, ionophore, and additive, respectively. The ionophore extracts a potassium ion into the hydrophobic core, which displaces a proton and deprotonates the chromoionophore. The chromoionophore's absorbance spectrum depends on protonation, which, in the nanosensor construct, becomes ion-specific optical change.

Most optode nanosensors use Nile red derivatives[8] for fluorescence measurements because of the dye's stability and ratiometric readout, however rapid photobleaching restricts imaging conditions to short durations or low excitation intensities. Imaging rapid ion fluxes requires short exposure times and, consequently, high-intensity illumination to achieve a reasonable signal-to-noise ratio[7c]. Replacing organic dyes with semiconductor quantum dots (QDs) has been shown to improve photostability of optodes[7e, 8c], but the optical interactions leading to a ratiometric response of these ion nanosensors remain poorly understood.

Here, we design a ratiometric potassium-selective nanosensor based on two QD species (Figure 1 schematic). A non-fluorescent chromoionophore responds dynamically to potassium by changing its absorbance spectrum and the strength of its interactions with either QD species (Figure 1 graph). By characterizing the analytical and physical properties, we confirm that the nanosensor functions through Förster resonant energy transfer (FRET) interactions between the QDs and the non-fluorescent chromoionophore. Using time-resolved photoluminescence spectroscopy we show that FRET mechanism is generalizable across QD-chromoionophore combinations, which is in agreement with their measured potassium sensing properties. Furthermore, *in vitro* experiments with live cells indicate that the nanosensors maintain their potassium sensitivity in physiological environments.

Results

To obtain ratiometric QD-based potassium sensors, QD490 and QD640 were selected because their fluorescence spectra (Figure 1, solid lines on spectra) overlap well with chromoionophore II (CHII) absorbance (Figure 1, dashed lines on spectra) and are completely non-overlapping with each other. The sonication-evaporation process is modified from previous work[8c] to more efficiently encapsulate QDs and optode components into bis(2-ethylhexyl) sebacate (also refered to as dioctyl sebacate, DOS) nanoemulsions stabilized by the PEGylated phospholipid DSPE-mPEG(550). Filtering the crude product with a syringe filter isolates a nanosensor population of 77 ± 21 nm diameter, as measured by dynamic light scattering (DLS) and a ζ-potential of −29 ± 7.6 mV.

High-resolution transmission electron microscope (TEM) images show globular nanosensors on TEM grids, with many particles containing a small number of QDs and some particles being void of QDs (Figure 2a). The overall population median diameter measured at 63 ± 30 nm, while the mean diameter for a subset of particles that contain two or more QDs measured 49 ± 17 nm (Figure 2b). Neither population approximates normality according to a Shapiro-Wilk test or D'Agnostino test. The two populations are significantly different according to the non-parametric Kolmogorov-Smirnov test ($p<0.0001$) between the two populations. The mean diameters measured by TEM are based on measuring the physical particle size while DLS measurements are based on scattering intensity and they measure the hydrodynamic radius. These technique differences explain the small discrepancy in mean diameters measured by TEM and DLS.

The nanosensors respond sensitively to potassium in accordance with established optode behavior (Equations 1–3). The ratiometric response (Equation 4) to potassium fits the Hill equation (Equation 5) with a half-maximal effective concentration (EC_{50}) of 24 mM ± 4 mM (Figure 3a–b, Figure S1a), lower and upper limits of detection at 1 and 590 mM, respectively, and a linear range from 2 to 120 mM. The nanosensor sensitivity, defined as the slope of the response at the EC_{50} measured −37% per log[K^+], and the ratiometric signal decreases by 10% between 4 – 8 mM. Nanosensors are stable for room-temperature storage through 7 days, as the EC_{50} only shifted to 36 ± 11 mM on Day 7 (Figure S2).

Nanosensors respond selectively for potassium over sodium, showing an EC_{50} for sodium >1 M (Figures 3a–b, Figure S1b) which produces a selectivity coefficient of 1.7 (Equation 5,

zero background ion). In 150 mM background sodium, the nanosensors have an EC_{50} of 34 ± 7 mM for potassium (Figure S3), a slope of −29% per log[K^+], and a ratiometric signal decrease of 9% from 4 – 8 mM. A selectivity coefficient is incalculable in 150 mM background potassium, because the nanosensors do not respond to sodium concentration changes in 150 mM potassium (Equation 5), or even in 50 mM background potassium (Figure S4a–b). Together these data show that nanosensors are stable, sensitive, and selective for potassium.

Nanosensor fluorescence responses to potassium (Figure 3a–b, Figure S1a–b) are consistent with absorbance changes reflecting the chromoionophore's protonation state (Figure S1c–d). As potassium concentration increases, CHII becomes deprotonated and its shorter absorbance peak increases while its longer absorbance peak decreases (Figure S1c–d). As the CHII absorbance overlapping with QD490 increases, QD490 fluorescence decreases, and vice-versa for QD640. Nanosensors made without the chromoionophore exhibit no potassium-dependent responses while nanosensors made with the chromoionophore clearly exhibit potassium-specific responses (Figure S5a–b). Thus the chromoionophore's protonation state determines the ratiometric response and is modulated by selective potassium exchange.

Studying deconstructed nanosensor formulations (Supplementary Table 1) delineates the photonic interactions between all three optical components – CHII and two QDs. Steady-state absorbance spectra show that 0 and 2 M potassium, respectively, fully protonates and deprotonates CHII (Figure 4d–f, dashed lines). In the absence of CHII, the steady-state fluorescence intensities from both QDs increase between 0 and 2 M KCl (Figure 3a–c). Formulations with CHII show CHII-mediated fluorescence changes; QD490 decreases intensity while QD640 increases intensity between 0 and 2 M KCl (Figure 3e–g).

To investigate the physical mechanism of the observed fluorescence changes, we measured FRET rates (Equation 8) between the components of optode using time-resolved spectroscopy (set up shown in Figure S6, streak camera images shown in Figure S7a–i). Consistent with observations of FRET in multi-QD systems[9], we find that fluorescence lifetime increases from 20 ns to 26 ns for QD640 and decreases from 19 to 17 ns for QD490 in a two-QD optode as compared to single-QD composites (Figure S8a–b, Table 1). We find that potassium concentration changes have no measurable effect on QD fluorescence lifetimes in the absence of CHII (Figure 5a–b, Figure S8a–c), indicating that FRET rate between QD490-QD640 pair is independent of potassium concentration. This constant QD490-QD640 FRET rate of $6.5*10^6$ s^{-1} (Figure 4b) was carried through transfer rate calculations for formulations with CHII.

As expected, deconstructed formulations containing CHII show that its protonation state strongly influences energy transfer from either QD to CHII. Between 0 and 2 M potassium, which corresponds to conditions in which CHII is fully protonated and deprotonated, respectively, QD490 to CHII transfer increases while QD640 to CHII transfer decreases (Figure 5, Table 2). In fact, QD fluorescence lifetimes change predictably over the potassium calibration panel, with QD490 lifetime gradually decreasing and QD640 lifetime gradually increasing with increasing potassium concentration (Figure S9a–c). Steady-state

fluorescence intensity measurements also reflect these CHII protonation-dependent results (Figure 3e–g, Figure S5a), and formulations made without CHII show no steady-state response to a potassium calibration panel (Figure S5b). These results show that changes in the aggregate CHII state are responsible for potassium-dependent changes in QD fluorescence through changes in FRET rate.

To further investigate the energy transfer processes within the nanosensors, the FRET radii were calculated for the protonated and deprotonated CHII cases. For these calculations we used experimentally determined PLQY of 0.64 and 0.42 for QD640 and QD490, respectively. The resulting FRET radii for protonated CHII-QD490 and CHII-QD640 are 2.77 and 6.24 nm, respectively, and those radii change to 4.39 and 2.82 nm, respectively, for deprotonated CHII (Figure S10). We define d_0 as the optimal separation distance between a QD and CHII to achieve the largest difference in FRET efficiency between the protonated and deprotonated states. For QD490-CHII, d_0 is 3.49 nm and for QD640-CHII, d_0 is 4.19 nm (Figure S11a–b). Using the optimal radii in the calculation of relative transfer rates (Equation 13), we find that the QD490-CHII FRET rate can maximally increase by a factor of 16 and the QD640-CHII transfer rate can maximally decrease by a factor of 118 (Equation 14) upon protonation/deprotonation. By comparison, time-resolved photoluminescence measurements show 3.1- and 4.2-fold changes in transfer rates for QD490-CHII and QD640-CHII, respectively (Figure 5b), indicating that the existing spacing between the QD donors and CHII acceptor is not optimal. The optimal distance for QD490-QD640 FRET radius was determined to be 3.52 nm, and the mean center-to-center distance calculated from time-resolved spectroscopy QD490-QD640 is 5.87 nm.

Since the platform is modular and no covalent conjugations are necessary to change the spectral properties of the emission dyes, the same optode cocktail can be used with many unique QD combinations. For example, nanosensors with QD540 and QD640 respond with two dynamic channels and an EC_{50} of 55 ± 4 mM (Figure S13a–b). Alternatively, pairing QD560 and QD640 produces a nanosensor with one static signal and one dynamic signal, and the ratiometric signal responds with an EC_{50} of 27 ± 7 mM and a slope of 39% per log[K^+] (Figure S14a–b). As long as one QD acts as a nanoantenna and at least one QD transfers to the chromoionophore's dynamic portion of its spectrum, the nanosensors' spectral properties are highly tunable.

Nanosensors imaged in controlled conditions exhibited full reversibility (Figure S15a–b, Video S1) and an EC_{50} of 24 ± 5 mM for the ratiometric measurement (Figure S16a–b). To assess the utility of our nanosensors in physiological environments we incubated them with HEK-293 cells. We find that nanosensors are distributed almost exclusively on the cell periphery (Figure 6a–c) and they respond to *in situ* calibrations with an EC_{50} of 40 mM (Figure 6d). While there is significant variability in photoluminescence intensity of individual QD spectra (Figure S17), the ratiometric signal shows a clear concentration-dependent response to potassium in phosphate buffered saline (PBS).

A similar experiment using a micro-injector to simulate a localized potassium source by delivering a quick, gentle puff of 150 mM potassium solution produced a rapidly reversible nanosensor response. The timing-matched image sets, acquired separately for each QD

spectral channel, show that photoluminescence intensity decreases for QD490 and increases for QD640 in response to an increase potassium concentration (Figure S18). This yields to a brief decrease of the ratio of fluorescence intensities QD490:QD640 (Figure 6f). The short, gentle puff of the pipette solution avoided introducing motion artifacts into the region of interest (Figure 6e, yellow oval), and the pipette had no positive pressure before or after the puff. This approach dilutes the pipette solution to an unknown potassium concentration less than the original 150 mM, but these measurements still demonstrate that nanosensors can detect a brief, small, and local increase in potassium concentration.

Discussion

We designed a bright, stable, and sensitive ratiometric nanosensor to address the challenges associated with imaging potassium in real-time. Of the existing small molecule indicators, only PBFI can quantitatively image potassium concentrations. It requires 340 and 380 nm excitation, exhibits low quantum yields of 0.04–0.08, and absorbs with an extinction coefficient of 45,000 (M^{-1} cm^{-1})[10]. The remaining indicators such as Asante Potassium Green (analogues exist for sodium as well)[6a, 6b, 10–11] are significantly brighter, but none are ratiometric. Given that ratiometric indicators more accurately quantify ion concentrations than single wavelength indicators,[12] a new family of bright and ratiometric ion indicators would be valuable research tools.

The QD490-QD640 nanosensor formulation responds sensitively to potassium and can measure potassium throughout the entire physiologic range (Figure 2a–b). Combinations of QD540-QD640 and QD560-QD640 demonstrated similarly sensitive and physiologically-relevant ratiometric responses (Figure S13a–b, Figure S14a–b). For this study, FRET rates and radii were calculated only for QD490-QD640 sensors, but the same approach translates to other QD combinations and it presents a rational route towards optimizing a nanosensors formulation, an approach that had not been described in QD-based, ion-selective nanosensors until now.

Basal potassium and sodium are 4 mM and 140 mM, respectively, and this high background sodium interferes with potassium measurements. The observed 50-fold selectivity for potassium over sodium makes this QD-based potassium sensors compare favorably to previously reported sensor designs[13]. Although small-molecule indicators have progressed significantly[4a, 14], QD resistance to photobleaching and narrow emission spectra make them appealing reporter components. More importantly, this dual-QD system produces a quantifiable ratiometric signal that responds to potassium calibrations with an identical EC_{50} of 24 mM in a well-plate calibration and in close proximity to the cell membrane.

The *in vitro* experiments indicate that HEK-293 cells do not internalize the nanosensors (Figure 6d, Figure S17). Any nanosensors sequestered in endosomes would not have responded to the *in situ* calibration and diminished the overall sensitivity. The passive external attachment mechanism is unknown at this point, but the high concentration of nanosensors during the incubation period and strong ζ-potential[15] may explain the phenomenon. In the future, nanosensors formulations will be targeted using peptides or other groups to specifically label cells of interest as other groups have done[16]. Altogether, these

results show that nanosensors are capable of sensitively responding to rapid changes in potassium concentration in physiologically-relevant conditions.

Conclusions

We aimed to design and characterize nanosensors capable of making real-time potassium concentration measurements in the physiological environment. The results show that optodes incorporating QDs have the sensitivity and selectivity to detect potassium in conditions of low and high interference from sodium. Measuring steady-state and time-resolved optical properties provided conclusive evidence that FRET between all three optically active elements is necessary for a dynamic ratiometric signal. Comparing the FRET rates from fluorescence lifetime measurements and overlap integral calculations showed that optimizing the FRET donor-acceptor distance will produce even more sensitive nanosensors. Finally, controlled *in situ* calibrations demonstrated that the nanosensors sensitively respond to potassium over concentration ranges corresponding to physiologic conditions. Future work will fine-tune formulations to achieve greater sensitivity by maximizing the number of particles that contain two or more quantum dots and apply these nanosensors to image potassium efflux from cells during signaling events.

Materials and methods

Materials

Bis(2-ethylhexyl) sebacate (DOS), chromoionophore II (CHII, 9-Dimethylamino-5-[4-(16-butyl-2,14-dioxo-3,15-dioxaeicosyl)phenylimino]benzo[a]phenoxazine, ETH 2439), potassium ionophore III (KI3, 2-Dodecyl-2-methyl-1,3-propanediyl bis[*N*-[5′-nitro(benzo-15-crown-5)-4′-yl]carbamate]), Sodium tetrakis[3,5-bis(trifluoromethyl)phenyl]borate (NaBARF), 4-(2-Hydroxyethyl)piperazine-1-ethanesulfonic acid (HEPES), sodium chloride (NaCl), dichloromethane (DCM) and tetrahydrofuran (THF) were purchased from Sigma-Aldrich. Quantum dots were purchased from NN-Labs (emission peak 640 nm, CZ640) and Cytodiagnostics (emission peak 490 nm, FN-490). Tris Base was purchased from Fisher BioReagents. Spectra/Por *in vivo* micro-dialysis hollow fibers (inner diameter 200 μm; outer diameter 280 μm, MWCO 13 kD) were purchased from Spectrum Labs, Inc. 1,2-distearoyl-*sn*-glycero-3-phosphoethanolamine-N-[methoxy(polyethylene glycol)-550] (ammonium salt) (DSPE-mPEG550) was purchased from Avanti Polar Lipids, Inc.

Nanosensor fabrication

Quantum dots were flocculated from chloroform by mixing as-received stocks in anhydrous methanol at a volume ratio of 4:1 MeOH:$CHCl_3$ and centrifuging for 5 minutes at 5000 × g. After repeating the wash and centrifugation steps three times, the quantum dots were resuspended in THF and their concentration was determined based on absorbance. The sensing components KI3 (4 μmol, 2 mg), CHIII (1.36 μmol, 1 mg), and NaTFPB (13.5 μmol, 12 mg) were reconstituted separately with THF and combined in a 2 mL glass vial so that the total THF volume was 300 μL. DOS (428 μmol, 200 μL) was added to the sensing components and vortexed briefly to homogenize the mixture. Just prior to nanosensor

fabrication, 5 mg of DSPE-mPEG550 was dried in a glass scintillation vial and reconstituted in 400 μL of DCM. 50 μL of the optode stock. 189 μg of QD490 and 182 μg of QD640 were added to the mixture. 4 mL of aqueous buffer (10 mM HEPES buffer; 6 mM tris base) was added and the mixture was sonicated for 1 minute with a Branson digital sonifier (S-450D) at 10% intensity with a 1/8″ diameter tip. After sonication, the organic solvents were removed using a rotavap (Buhle) for 10 minutes at room temperature. The resulting emulsion was filtered with a 100 nm syringe filter.

Particle size and zeta-potential measurements

Hydrodynamic diameters were measured by dynamic light scattering (DLS) using a 90 Plus particle size analyzer by Brookhaven Instruments Corporation. All particle size measurements were taken in triplicate by diluting the sample solution in 10 mM HEPES buffer, pH-7.2 so that the detector count rate measured 50 – 450 kcps. The detector measured scattered 640 nm light at a fixed angle of 90°, and calculated the effective diameter based on the intensity of scattered light. Zeta-potentials were measured using the same 90 Plus instrument in PALS mode. Sample concentrations were adjusted until the detector count rate measured 100 – 450 kcps and then 25 cycles of 10 runs per cycle were collected. Three batches of nanosensors each from two separate stock optode preparations were measured.

Electron Microscopy

Diluted samples of the PUNQs were air-dried onto 300-mesh carbon film-coated copper grids (Electron Microscopy Sciences). The grid was washed three times with distilled water, placed onto a 5 μL drop of 1.5% phosphotungstic acid stain for 5 minutes, and dried with filter paper to remove excess liquid. Images were acquired at 120 kV accelerating voltage on an FEI Tecnai Multipurpose TEM. Images were analyzed using ImageJ to measure nanoparticle diameters. Diameters were tested for normality using Shapir-Wilk and D'Agostino & Pearson tests. Both tests indicated non-normal distributions population differences were tested with Kolmogorov-Smirnov non-parametric test. Statistical analysis was conducted using GraphPad Prism.

Fluorescent response to potassium

Nanosensors were calibrated for their fluorescent response to potassium in 10 mM HEPES buffer, pH 7.2. The responses are described by optode theory[17] for ion-exchange in a system described at equilibrium by:

$$I^{z+}(aq) + n\mathrm{L}(\mathrm{org}) + z\mathrm{C}H^{+} \leftrightarrow I\mathrm{L}_{n}^{z+}(\mathrm{org}) + z\mathrm{C}(\mathrm{org}) + zH^{+}(aq) \quad \text{(Eq. 1)}$$

where I, L and C are the ion of interest, ionophore and chromoionophore, respectively, and *org* and *aq* denote an ion, *I*, in a component in the organic optode phase or the aqueous phase, respectively. The ion-exchange system then has an exchange constant to describe the partitioning between the two phases given by:

$$K_{\text{exch}}^{IL_n} = \left(\frac{a_H[\text{C}]}{[\text{C}H^+]}\right) \frac{^z\,[IL_n^{z+}]}{a_I[\text{L}]^n} = \left(\frac{K_a}{K_H}\right)^z k_I \beta_{IL_n} \quad \text{(Eq. 2)}$$

where the variables a_H and a_I denote the activity of a proton, H, or the ion in the sensor. Due to the electroneutrality condition, the optical activity reflects the concentration of the respective complexes within the organic nanosensor phase. Under those conditions, the relation between the nanosensor's protonation ratio (α) and ion activities is:

$$a_I = \left(zK_{\text{exch}}^{IL_n}\right)^{-1} \left(\frac{\alpha}{1-\alpha} a_H\right)^z \times \frac{R_T^- - (1-\alpha)\,C_T}{\left\{L_T - \left(R_T^- - (1-\alpha)\,C_T\right)\left(n/z\right)\right\}^n} \quad \text{(Eq. 3)}$$

For each calibration point, the nanosensor solution was mixed with standard solutions so that the final KCl concentrations were 10 – 150 mM KCl and solutions of 10 mM NaOH or 10 μM HCl were used to, respectively, fully deprotonate or protonate the chromoionophore in order to determine the fraction protonated during measurements in KCl. The fluorescence intensities for QD490 (ex: 405, em: 490) and QD640 (ex: 405, em: 650) were measured with Spectramax M3 plate reader (Molecular Devices) in bottom read mode through clear-bottom 96-well plates. The fluorescence ratio for QD640:QD490 was calculated as:

$$R = \frac{490\ \text{emission}}{640\ \text{emission}} \quad \text{(Eq. 4)}$$

The EC_{50}, for the nanosensors was calculated from the ratiometric values according to the dose-response (Hill) equation:

$$R = R_0 \frac{(R_1 - R_0)}{1 + 10^{\text{Log}(EC_{50} - x)p}} \quad \text{(Eq. 5)}$$

where R_0 and R_1 are the ratio values in conditions that fully protonate and deprotonate CHII, respectively. The Hill slope is p and x is a potassium concentration at which a ratio was measured.

Nanosensor selectivity was determined by measuring the fluorescent response to NaCl and fitting the calibration data to the Nicolskii-Eisenman model with a fixed interfering ion[7a, 18], which defines the selectivity coefficient for an optical sensor as:

$$\text{Log}K_{ij}^{\text{opt}} = \text{LogE}\,C_{50}^i - \text{LogE}\,C_{50}^j \quad \text{(Eq. 6)}$$

Where EC_{50}^i and EC_{50}^j are the EC_{50} constants for the interfering ion (sodium) and primary (potassium), respectively.

Nanosensor shelf-stability

In order to characterize the shelf-life for the nanosensors, their fluorescent response to potassium were evaluated over the course of 7 days. In triplicate, nanosensors were fabricated and stored at room temperature with no protection from ambient light. At days 0, 1, 2, 3, 6, and 7, aliquots were removed to produce a calibration curve in response to potassium and sodium. The calibration conditions were identical to those described in the previous section, and the results were fit to a dose-response model to calculate the EC_{50}.

Determination of fluorescence dynamics within nanosensors

Nanosensor formulations were fabricated using the emulsification method described above with the following combinations, in mg:

	DOS	CHII II	Ki3	NaBARF	QD490	QD640
CHII	10	0.05	0.4	1.2	0	0
QD490/QD640	10	0	0.4	1.2	0.1	0.1
QD490-CHII	10	0.05	0.4	1.2	0.1	0.1
QD640-CHII	10	0.05	0.4	1.2	0.1	0.1
QD490/QD640-CHII	10	0.05	0.4	1.2	0.1	0.1
QD490	10	0	0.4	1.2	0.1	0.1
QD640	10	0	0.4	1.2	0.1	0.1

The crude product from each combination was diluted 1:4 for the subsequent measurements. The absorbance spectra from 450 – 740 nm was recorded in 5 nm steps. Fluorescence spectra were recorded with 400 nm excitation, collected from 450 – 740 nm in 5 nm steps. The emission spectra were normalized with respect to the peak emission of QD490 for the formulation with only QD490.

Time-resolved fluorescent spectra were collected on a custom-built free-space optical system (Figure S6). Laser excitation of 400 nm at 1 kHz (Coherent Libra with OPerA) was focused into a quartz cuvette (Starna Cells) at a 45-degrees angle to minimize detection of reflected laser light. Emission was filtered with a 450 nm longpass filter (Thor Labs) and portion of the subsequent sample fluorescence was focused into the streak camera (Hamamatsu C5680) using simple optical re-image systems.

From the streak image, emission data of each QD donor was selected based on the full-width half-maximum of the photoluminescence (PL) spectrum. The resulting spectrally integrated time-resolve PL for each quantum dot was plotted on a semi-log scale and approximated using a single exponential. A fitting is performed for each QD emission from 3 ns – 40 ns after excitation to compute τ, the exciton lifetime:

$$I(t) = I_O e^{-t/\tau} \quad \text{(equation 7)}$$

where I(t) is the intensity of fluorescence detected at time, t, after a laser pulse and I_O is the fluorescence intensity at t=0. The exciton lifetime, **τ**, for donors is determined based on the rate of radiative (k_r), non-radiative recombination (k_{nr}), and energy transfer to lower energy QDs and/or acceptor molecules (k_{trans}):

$$\tau = k^{-1} = \frac{1}{k_r + k_{nr} + k_{\text{trans}}} \quad \text{(equation 8)}$$

Time-resolved spectra were recorded with full nanosensors in 0, 1, 4, 8, 20, 50, 100, 150, and 1000 mM KCl in 10 mM HEPES (pH = 7.4 with tris-base). Additionally, each formulation from Table 1 was placed in 0 or 2 M KCl and time-resolved fluorescent spectra were recorded with 400 nm excitation. To further examine the effects of QDs on fluorescence lifetime of CHII acceptors, fluorescent spectra were recorded for 0 M KCl with CHII, QD640-CHII and QD490/QD640-CHII from Table 1. In case of QD490/QD640-CHII, the CHII fluorescence was difficult to resolve from the strong QD signal, so time-resolved spectra were recorded from two formulations made with 0.02 mg of each QD and 0.004 mg of each QD in 0 M KCl.

The three-dimensional radius at which FRET is 50% efficient relative to its maximum, R_0^6, for each QD with CHII when CHII is protonated or deprotonated. CHII was dissolved into THF at a concentration of 54 μM and CHII absorption in both states were measured for the wavelength range of 350 – 800 nm in 1 nm steps using a UV-VIS-NIR spectrophotometer (Cary 5000). The absorption data is used to compute the molar absorptivity, $\varepsilon_A(\lambda)$ based on the Beer-Lambert Law:

$$\varepsilon_A(\lambda) = \frac{-ln\left(\frac{I}{I_0}\right)}{lc} = \frac{-ln(1 - \text{Abs}(\lambda))}{lc} \quad \text{(equation 9)}$$

Photoluminescent spectra for each QD in THF were taken using a fluorometer (Cary Eclipse) for the wavelength range of 350 – 800 nm in 1 nm steps and normalized according to:

$$f_D(\lambda) = \frac{F_{D_\lambda}(\lambda)}{\int F_{D_\lambda}(\lambda)\, d\lambda} \quad \text{(equation 10)}$$

The overlap integral, *J*, was computed using the CHII wavelength-dependent and protonation-dependent molar extinction coefficients and the QD photoluminescent spectra:

$$J=\int f_D(\lambda)\,\varepsilon_A(\lambda)\,\lambda^4 d\lambda \quad \text{(equation 11)}$$

The FRET radius, R_0, was thus computed as:

$$R_0^6=\frac{9\,(ln\,(10))\,\kappa^2\Phi_D J}{128\pi^5 n^4 N_A} \quad \text{(equation 12)}$$

where κ^2 is the dipole orientation factor (assumed to be 2/3 for isotropically oriented donor and acceptor), J is the overlap integral, n is the refractive index of DOS (1.45), Φ_D is the fluorescence quantum yield of the donor QD in the absence of CHII, and N_A is Avogadro's number. The predicted transfer rate is calculated according to:

$$K_T(r)=\frac{1}{\tau_D}\left(\frac{R_0}{r}\right)^6 \quad \text{(equation 13)}$$

where τ_D is the QD lifetime in the absence of CHII and r is the QD-CHII distance. The relative change in transfer rate between the protonated and deprotonated CHII case was calculated according to:

$$\frac{K_T^C(r)}{K_T^{CH+}(r)} \quad \text{(equation 14)}$$

where $K_R^C(r)$ and $K_R^{CH+}(r)$ are the transfer rates for the deprotated and protonated CHII cases, respectively

Reversibility with Confocal Microscope

Nanosensors were imaged with a laser scanning confocal microscope by immobilizing the nanosensors inside of a piece of sealed dialysis tubing that was fixed to a glass coverslip. The setup, described and demonstrated previously[7b], involved filling a 1.5 cm length of micro-dialysis tubing (ID: 200 μm, OD: 250 μm, 13kDa MWCO, Spectrum Labs) with nanosensors suspended in 10 mM HEPES buffer, sealed on its ends with fast-curing epoxy, and fixed to a 15 mm diameter circular glass coverslip with two drops of water-curing epoxy. No attempt was made to control or measure the concentration of nanosensors between batches. The glass coverslip was then secured in a flow chamber (Warner Instruments, RC-21BRFS) and mounted for imaging on a laser scanning confocal microscope (Zeiss LSM 700). A 405 nm laser (1% intensity, 5 mW full power excited both quantum dots simultaneously, and the two emissions were split with a diffraction grating set to split the emission at 580 nm. Images were acquired at 20 second intervals and the solutions were changed every 3 minutes - alternating between 10 and 100 mM KCl in 10 mM HEPES, pH 7.2 with tris base.

Images were analyzed with the Fiji[19] plugin suite of ImageJ (NIH) with the region of interest defined as the interior of the dialysis tube and the region of interest definitions for both channels were identical.

Calibration With a Confocal Microscope

Nanosensors were immobilized in dialysis tubing as described above and mounted in a perfusion chamber for imaging on a confocal microscope. Solutions of 0, 4, 8, 20, 50, 100, 150, and 1124 mM KCl were perfused through the chamber and three images were acquired at each of the eight concentrations measured. Nanosensors were excited with a 405 nm laser set to 1.1% intensity (5 mW full power). For image analysis, a thresholded mask was created using Otsu's method and the mean channel value for QD490 and QD640 were measured separately and the ratio of QD490:QD640 fluorescence was calculated and fit to a dose-response curve.

In situ calibration and response to exogenous KCl in cellular environment

In situ calibrations were performed on HEK-293 cells (ATCC) cultured on 25 mm glass coverslips. Exogenous KCl application was performed on HEK-293 cells cultured on glass-bottom dishes (Mat-tek). Growth medium contained 89% DMEM, 10% FBS, and 1% Pen-strep and cells were cultured for three days after plating. One hour prior to imaging, cell culture medium was aspirated out of a glass bottom dish and replaced with nanosensors in PBS, 2 mM $CaCl_2$, 1.2 mM $MgCl_2$, and 10 mM glucose and allowed to incubate for an hour at 37°C. After one hour, the cells were rinsed three times with PBS and then moved to an upright microscope (Zeiss AxioObserver) for imaging with a 40× oil immersion objective (NA=1.3).

For calibrations, 10× PBS (Boston BioProducts) was spiked with additional KCl to bring the final KCl concentration to 4, 8, 16, 20, 50, 100, and 150 mM KCl in 1× PBS. Cells cultured on glass coverslips were mounted in a perfusion chamber and 3 images were acquired in each condition using a 405 laser set to 0.6 – 0.9% power (5 mW full power). A diffraction grating split the emission at 580 nm and 2 channels were collected, one for QD490 and one for QD640 fluorescence. In each solution, 3 images were collected for each channel.

Images were analyzed in Fiji/ImageJ (NIH). First, the three images were averaged, and then a binary mask was generated based on Otsu's method for thresholding on the QD640 channel. An image based on the pixel-wise ratio of QD490:QD640 was also generated, and the region within the mask was measured for both channels and the ratiometric channel. The mean channel intensities were tabulated and averaged in each solution condition to produce a calibration curve for the nanosensors when they are attached to cells and in physiologic solutions.

To apply exogenous KCl, a pulled glass micropipette (1 mm OD, 0.5 mm ID, Sutter) was filled with 150 mM KCl in 10 mM HEPES (pH=7.4 with 6 mM Tris base) and brought into close proximity with a cell without any positive pressure on the pipette. An imaging sequence was initiated and controlled with digital logic in pClamp 10.4 (Molecular Devices). The microscope epifluorescence shutter was opened, and then 300 ms of frames were recorded with 50 ms exposures (Hamamatsu Flash 4.0) before a gentle 200 ms puff of

KCl from the pipette tip was delivered. The sequence was first recorded with a GFP filter set (Ex: 470/40; BS: 495; Em: 525/50) and then with a Cy3 filter set (Ex: 545/25; BS: 570; Em: 605/70).

Supplementary Material

Refer to Web version on PubMed Central for supplementary material.

Acknowledgments

The authors thank Dr. Zhang (Jane) Wang for help with figure preparation

Funding Sources

TTR, CGS, and HAC are supported by R01NS081641. TTR is supported by F32EB015847, CGS is supported by

References

1. (a) Ruckh TT, Mehta AA, Dubach JM, Clark HA. Polymer-free optode nanosensors for dynamic, reversible, and ratiometric sodium imaging in the physiological range. Scientific reports. 2013; 3:3366. [PubMed: 24284431] (b) Rose CR. Two-photon sodium imaging in dendritic spines. Cold Spring Harb Protoc. 2012; 2012(11):1161–5. [PubMed: 23118361]
2. Milstein ML, Musa H, Balbuena DP, Anumonwo JM, Auerbach DS, Furspan PB, Hou L, Hu B, Schumacher SM, Vaidyanathan R, Martens JR, Jalife J. Dynamic reciprocity of sodium and potassium channel expression in a macromolecular complex controls cardiac excitability and arrhythmia. Proc Natl Acad Sci USA. 2012; 109(31):E2134–43. [PubMed: 22509027]
3. (a) Lansu K, Gentile S. Potassium channel activation inhibits proliferation of breast cancer cells by activating a senescence program. Cell Death Dis. 2013; 4:e652. [PubMed: 23744352] (b) Lee I, Lee SJ, Kang TM, Kang WK, Park C. Unconventional role of the inwardly rectifying potassium channel Kir2.2 as a constitutive activator of RelA in cancer. Cancer Res. 2013; 73(3):1056–62. [PubMed: 23269273] (c) Bodenstine TM, Vaidya KS, Ismail A, Beck BH, Diers AR, Edmonds MD, Kirsammer GT, Landar A, Welch DR. Subsets of ATP-sensitive potassium channel (KATP) inhibitors increase gap junctional intercellular communication in metastatic cancer cell lines independent of SUR expression. FEBS Lett. 2012; 586(1):27–31. [PubMed: 22119728]
4. (a) Kamiya M, Johnsson K. Localizable and highly sensitive calcium indicator based on a BODIPY fluorophore. Anal Chem. 2010; 82(15):6472–9. [PubMed: 20590099] (b) Tour O, Adams SR, Kerr RA, Meijer RM, Sejnowski TJ, Tsien RW, Tsien RY. Calcium Green FlAsH as a genetically targeted small-molecule calcium indicator. Nat Chem Biol. 2007; 3(7):423–31. [PubMed: 17572670]
5. (a) Akerboom J, Chen TW, Wardill TJ, Tian L, Marvin JS, Mutlu S, Calderon NC, Esposti F, Borghuis BG, Sun XR, Gordus A, Orger MB, Portugues R, Engert F, Macklin JJ, Filosa A, Aggarwal A, Kerr RA, Takagi R, Kracun S, Shigetomi E, Khakh BS, Baier H, Lagnado L, Wang SS, Bargmann CI, Kimmel BE, Jayaraman V, Svoboda K, Kim DS, Schreiter ER, Looger LL. Optimization of a GCaMP calcium indicator for neural activity imaging. J Neurosci. 2012; 32(40): 13819–40. [PubMed: 23035093] (b) Muto A, Ohkura M, Kotani T, Higashijima S, Nakai J, Kawakami K. Genetic visualization with an improved GCaMP calcium indicator reveals spatiotemporal activation of the spinal motor neurons in zebrafish. Proc Natl Acad Sci USA. 2011; 108(13):5425–30. [PubMed: 21383146] (c) Mank M, Santos AF, Direnberger S, Mrsic-Flogel TD, Hofer SB, Stein V, Hendel T, Reiff DF, Levelt C, Borst A, Bonhoeffer T, Hubener M, Griesbeck O. A genetically encoded calcium indicator for chronic in vivo two-photon imaging. Nat Methods. 2008; 5(9):805–11. [PubMed: 19160515]
6. (a) Lamy CM, Sallin O, Loussert C, Chatton JY. Sodium sensing in neurons with a dendrimer-based nanoprobe. ACS Nano. 2012; 6(2):1176–87. [PubMed: 22288942] (b) Kim MK, Lim CS, Hong JT, Han JH, Jang HY, Kim HM, Cho BR. Sodium-ion-selective two-photon fluorescent probe for in vivo imaging. Angew Chem Int Ed Engl. 2010; 49(2):364–7. [PubMed: 19998298] (c) Scelfo B,

Strata P, Knopfel T. Sodium imaging of climbing fiber innervation fields in developing mouse Purkinje cells. Journal of neurophysiology. 2003; 89(5):2555–63. [PubMed: 12612029] (d) Knopfel T, Anchisi D, Alojado ME, Tempia F, Strata P. Elevation of intradendritic sodium concentration mediated by synaptic activation of metabotropic glutamate receptors in cerebellar Purkinje cells. The European journal of neuroscience. 2000; 12(6):2199–204. [PubMed: 10886360] (e) Callaway JC, Ross WN. Spatial distribution of synaptically activated sodium concentration changes in cerebellar Purkinje neurons. Journal of neurophysiology. 1997; 77(1):145–52. [PubMed: 9120555]

7. (a) Bakker E, Simon W. Selectivity of ion-sensitive bulk optodes. Analytical Chemistry. 1992; 64(17):1805–1812.(b) Balaconis MK, Clark HA. Biodegradable optode–based nanosensors for in vivo monitoring. Anal Chem. 2012; 84(13):5787–93. [PubMed: 22725692] (c) Dubach JM, Das S, Rosenzweig A, Clark HA. Visualizing sodium dynamics in isolated cardiomyocytes using fluorescent nanosensors. Proc Natl Acad Sci USA. 2009; 106(38):16145–50. [PubMed: 19805271] (d) Harjes DI, Dubach JM, Rosenzweig A, Das S, Clark HA. Ion-selective optodes measure extracellular potassium flux in excitable cells. Macromolecular rapid communications. 2010; 31(2): 217–21. [PubMed: 21590894] (e) Xu C, Bakker E. Multicolor quantum dot encoding for polymeric particle-based optical ion sensors. Anal Chem. 2007; 79(10):3716–23. [PubMed: 17437337] (f) Xu C, Wygladacz K, Retter R, Bell M, Bakker E. Multiplexed flow cytometric sensing of blood electrolytes in physiological samples using fluorescent bulk optode microspheres. Anal Chem. 2007; 79(24):9505–12. [PubMed: 18001125]
8. (a) Clark HA, Hoyer M, Philbert MA, Kopelman R. Optical nanosensors for chemical analysis inside single living cells. 1. Fabrication, characterization, and methods for intracellular delivery of PEBBLE sensors. Anal Chem. 1999; 71(21):4831–6. [PubMed: 10565274] (b) Clark HA, Kopelman R, Tjalkens R, Philbert MA. Optical nanosensors for chemical analysis inside single living cells. 2. Sensors for pH and calcium and the intracellular application of PEBBLE sensors. Anal Chem. 1999; 71(21):4837–43. [PubMed: 10565275] (c) Dubach JM, Harjes DI, Clark HA. Ion-selective nano-optodes incorporating quantum dots. Journal of the American Chemical Society. 2007; 129(27):8418–9. [PubMed: 17567136]
9. (a) Kagan CR, Murray CB, Bawendi MG. Long-range resonance transfer of electronic excitations in close-packed CdSe quantum-dot solids. Physical review B, Condensed matter. 1996; 54(12):8633–8643.(b) Achermann M, Petruska MA, Crooker SA, Klimov VI. Picosecond Energy Transfer in Quantum Dot Langmuir−Blodgett Nanoassemblies. The Journal of Physical Chemistry B. 2003; 107(50):13782–13787.(c) Lunz M, Bradley AL, Chen W-Y, Gun'ko YK. Two-Dimensional Förster Resonant Energy Transfer in a Mixed Quantum Dot Monolayer: Experiment and Theory. The Journal of Physical Chemistry C. 2009; 113(8):3084–3088.
10. Minta A, Tsien RY. Fluorescent indicators for cytosolic sodium. J Biol Chem. 1989; 264(32): 19449–57. [PubMed: 2808435]
11. Rimmele TS, Chatton JY. A novel optical intracellular imaging approach for potassium dynamics in astrocytes. PloS one. 2014; 9(10):e109243. [PubMed: 25275375]
12. Thestrup T, Litzlbauer J, Bartholomaus I, Mues M, Russo L, Dana H, Kovalchuk Y, Liang Y, Kalamakis G, Laukat Y, Becker S, Witte G, Geiger A, Allen T, Rome LC, Chen TW, Kim DS, Garaschuk O, Griesinger C, Griesbeck O. Optimized ratiometric calcium sensors for functional in vivo imaging of neurons and T lymphocytes. Nat Methods. 2014; 11(2):175–82. [PubMed: 24390440]
13. (a) Singh N, Mulrooney RC, Kaur N, Callan JF. Fluorescent recognition of potassium and calcium ions using functionalised CdSe/ZnS quantum dots. Journal of fluorescence. 2009; 19(5):777–82. [PubMed: 19330431] (b) Chen CY, Cheng CT, Lai CW, Wu PW, Wu KC, Chou PT, Chou YH, Chiu HT. Potassium ion recognition by 15-crown-5 functionalized CdSe/ZnS quantum dots in H2O. Chemical communications. 2006; (3):263–5.(c) Ruedas-Rama MJ, Hall EA. K+-selective nanospheres: maximising response range and minimising response time. The Analyst. 2006; 131(12):1282–91. [PubMed: 17124535]
14. (a) Carpenter RD, Verkman AS. Synthesis of a sensitive and selective potassium-sensing fluoroionophore. Organic letters. 2010; 12(6):1160–3. [PubMed: 20148571] (b) Padmawar P, Yao X, Bloch O, Manley GT, Verkman AS. K+ waves in brain cortex visualized using a long-wavelength K+-sensing fluorescent indicator. Nat Methods. 2005; 2(11):825–7. [PubMed: 16278651] (c) Baruah M, Qin W, Vallee RA, Beljonne D, Rohand T, Dehaen W, Boens N. A

highly potassium-selective ratiometric fluorescent indicator based on BODIPY azacrown ether excitable with visible light. Organic letters. 2005; 7(20):4377–80. [PubMed: 16178537]

15. Cho EC, Xie J, Wurm PA, Xia Y. Understanding the role of surface charges in cellular adsorption versus internalization by selectively removing gold nanoparticles on the cell surface with a I2/KI etchant. Nano Lett. 2009; 9(3):1080–4. [PubMed: 19199477]
16. (a) Moon JJ, Suh H, Li AV, Ockenhouse CF, Yadava A, Irvine DJ. Enhancing humoral responses to a malaria antigen with nanoparticle vaccines that expand Tfh cells and promote germinal center induction. Proc Natl Acad Sci USA. 2012; 109(4):1080–5. [PubMed: 22247289] (b) Stephan MT, Moon JJ, Um SH, Bershteyn A, Irvine DJ. Therapeutic cell engineering with surface-conjugated synthetic nanoparticles. Nat Med. 2010; 16(9):1035–41. [PubMed: 20711198]
17. (a) Bakker E, Buhlmann P, Pretsch E. Carrier-Based Ion-Selective Electrodes and Bulk Optodes. 1. General Characteristics. Chem Rev. 1997; 97(8):3083–3132. [PubMed: 11851486] (b) Buhlmann P, Pretsch E, Bakker E. Carrier-Based Ion-Selective Electrodes and Bulk Optodes. 2. Ionophores for Potentiometric and Optical Sensors. Chem Rev. 1998; 98(4):1593–1688. [PubMed: 11848943]
18. Seiler K, Simon W. Theoretical Aspects of Bulk Optode Membranes. Anal Chim Acta. 1992; 266(1):73–87.
19. Schindelin J, Arganda-Carreras I, Frise E, Kaynig V, Longair M, Pietzsch T, Preibisch S, Rueden C, Saalfeld S, Schmid B, Tinevez JY, White DJ, Hartenstein V, Eliceiri K, Tomancak P, Cardona A. Fiji: an open-source platform for biological-image analysis. Nat Methods. 2012; 9(7):676–82. [PubMed: 22743772]

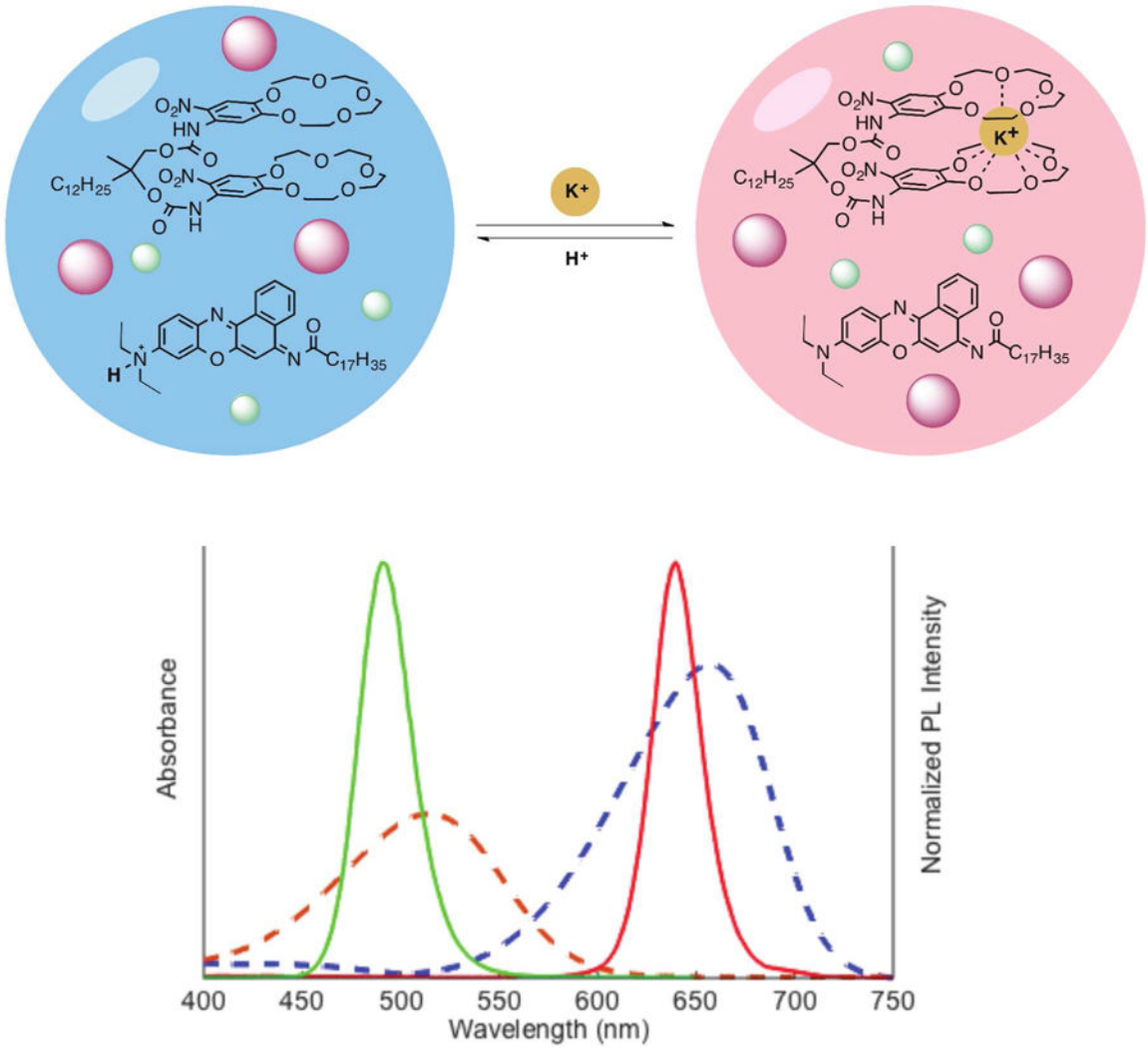

Figure 1.

Schematic of nanosensor's selective H^+/K^+ exchange (upper schematic). The chromoionophore's absorbance spectrum (bottom, dashed lines) changes depending on its protonation. Quantum dots (bottom, solid lines) are unaffected by pH or potassium concentration.

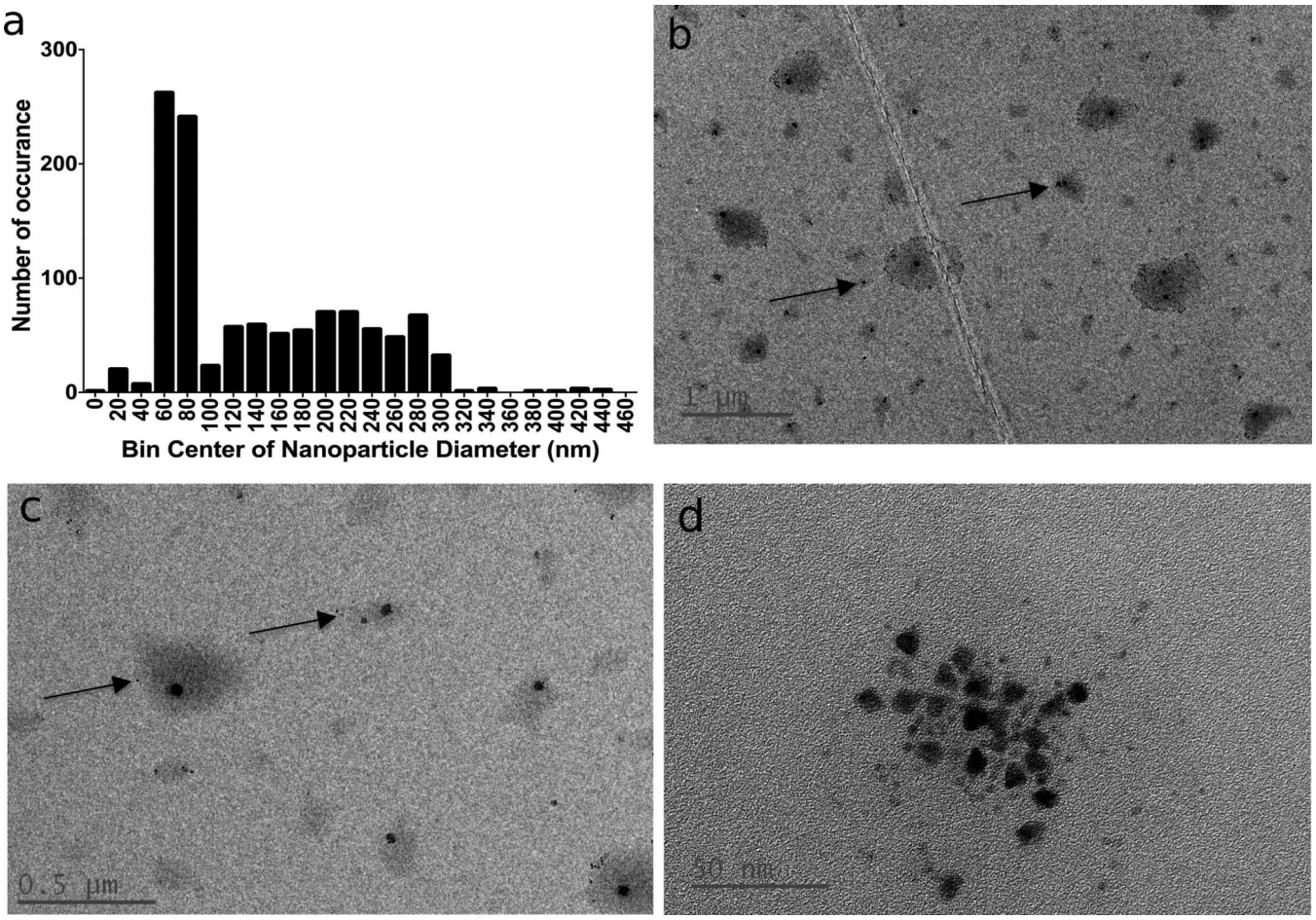

Figure 2.

High resolution TEM image of nanosensors (a); size distribution measurements of all particles measured and particles containing at least 2 QDs (b)

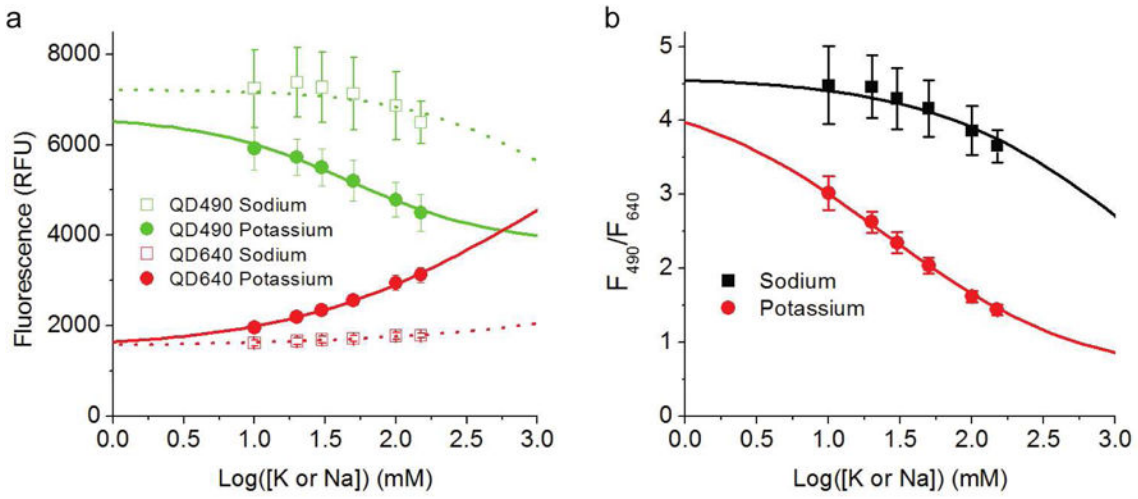

Figure 3.

Fluorescence calibration curves for individual QDs (a) and ratio (b) in response to sodium (□) or potassium (●). Error bars indicate one standard deviation

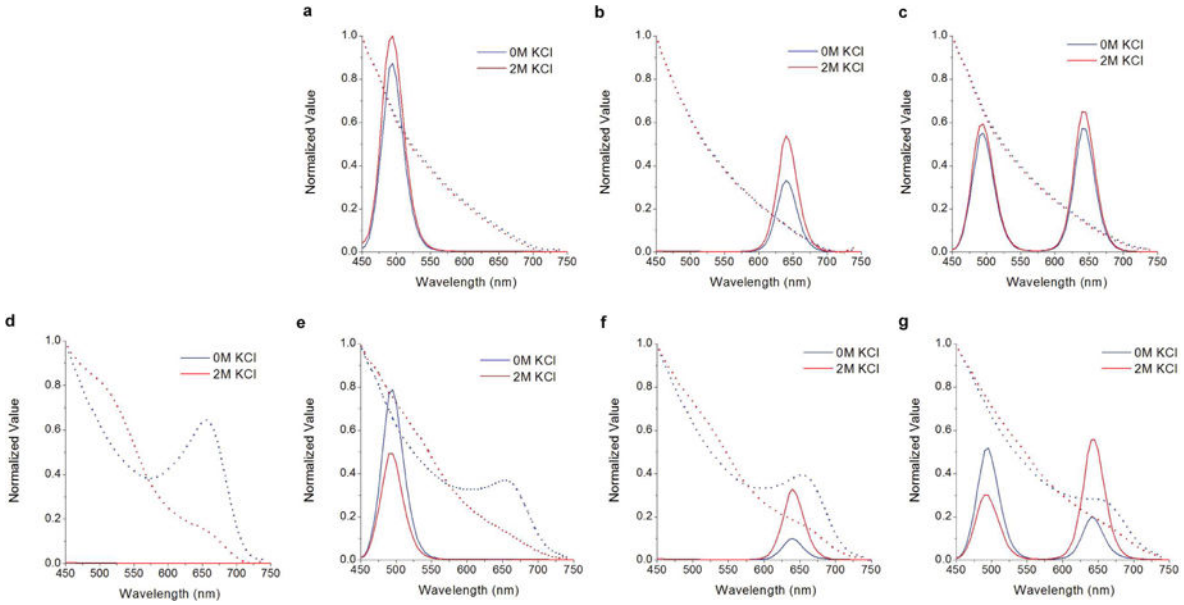

Figure 4.

Steady-state absorbance (dashed) and fluorescence (solid) spectra of deconstructed nanosensor components. Deconstructed nanosensors contain QD490 (a), QD640 (b), both QDs (c), QD490 and CHII (d), QD640 and CHII (e), and both QDs and CHII (f). Error bars indicate one standard deviation

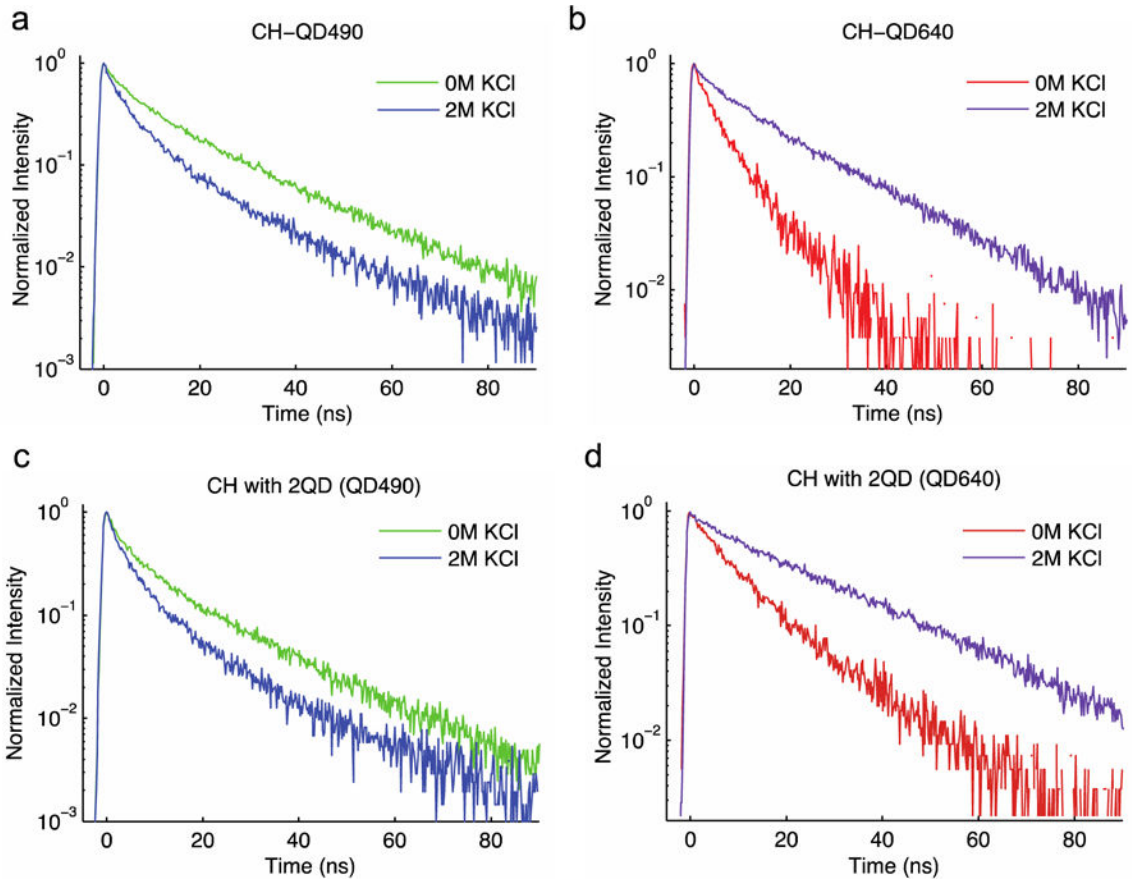

Figure 5.

Intensity-normalized time-resolved fluorescence of QDs showing potassium-dependent changes in QD lifetime for QD490 (c) and QD640 (d) when formulated with either QD alone. Intensity-normalized plots for QD490 (e) and QD640 (f) when formulated with both QDs.

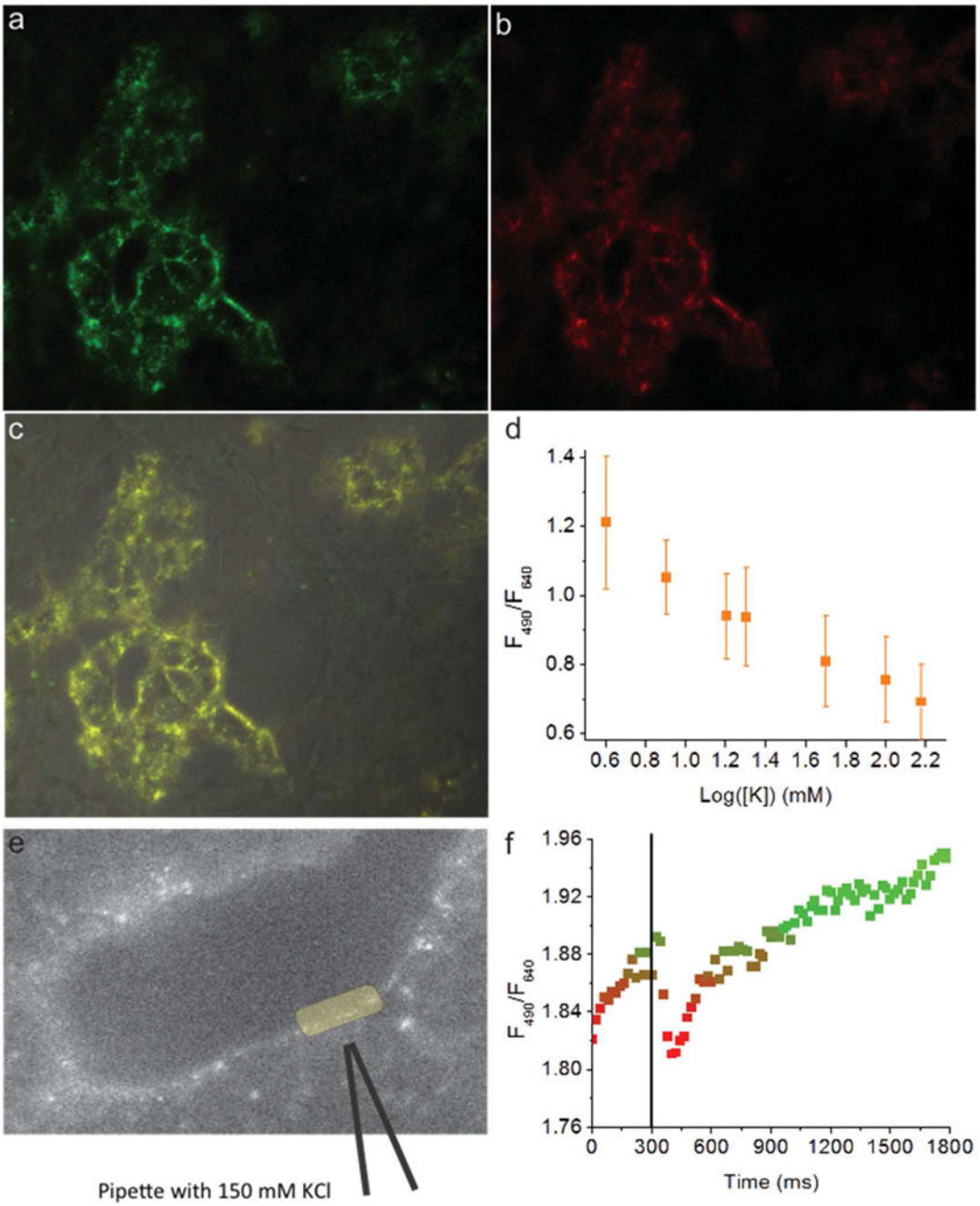

Figure 6.

Fluorescence images of HEK-293 cells coated with nanosensors showing QD490 fluorescence (a), QD640 fluorescence (b), merged channels (c), and *in situ* calibration results (d). HEK-293 cells coated with nanosensors (e) briefly exposed to KCl, and the ratiometric signal changes in response to the transient KCl exposure (f).

Table 1

Fluorescence decay time constants for deconstructed nanosensors. Each QD's lifetime in the formulation conditions

	τ (ns)	
	0 M	**2 M**
QD490	18.7	17.7
QD490 in 2QD	16.7	16.2
QD490 in (CH+2QDs)	14.7	11.2
QD490 in (CH+QD1)	16.3	12.3
QD640	19.6	20.1
QD640 in (2QDs)	25.9	26.1
QD640 in (CH+2QDs)	11.4	22.3
QD640 in (CH+QD1)	10.8	16.8

Table 2

Transfer rates for optical components within fully-formulated potassium-selective nanosensors. Conditions of 0 M KCl and 2 M KCl permit CHII to be fully protonated or fully deprotonated

	Transfer rates (1×10^6 s^{-1})	
	0 M	**2 M**
QD490-QD640	6.2	5.2
QD490-CHII	7.7	24.4
QD640-CHII	41.6	9.7